

A Spectroscopy-Constraint Network for Fast Thermochemical Process Monitoring Using Wavelength Modulation Spectroscopy

Jiangnan Xia, Rui Zhang, Ihab Ahmed, Mohamed Pourkashanian, Ian Armstrong, Michael Lengden, Walter Johnstone, Hugh McCann, and Chang Liu, *Senior Member, IEEE*

Abstract—Performance optimization of various combustion-based power generation systems requires fast and accurate online monitoring of their thermochemical parameters. As an *in situ* sensing technology, laser absorption spectroscopy (LAS) with modulated wavelength, has been widely adopted. However, rapid parameters retrieval from modulated LAS signal can be challenging due to the underlying complex and non-linear spectroscopy model. Most existing acceleration algorithms utilize supervised neural networks in an end-to-end manner ignored constraints on the spectroscopic model constraint. In addition, most state-of-the-art neural networks exhibit complicated structures with low computation efficiency. In this work, we developed a spectroscopy-constraint neural network for rapid thermochemical parameters extraction. The laser spectroscopic model is integrated in the proposed network through an encoder-decoder structure, offering independency on synthetic labeled dataset and hence enhance its performance on measurement thermochemical parameters in industrial scenarios. Furthermore, the developed network has a simple structure and lightweight parameter size. A case study of an aircraft engine exhaust monitoring is presented. The proposed model effectively reveals the dynamic behaviors of the engine. Compared with two representative supervised models, the new model exhibits better performance on spectral recovery as well as higher computational efficiency.

Index Terms—laser absorption spectroscopy; wavelength modulation spectroscopy; thermochemical parameters; neural networks; gas turbine engine.

I. INTRODUCTION

DYNAMIC process modelling [1-3] and intelligent control strategies [4, 5] can greatly improve operational performance of combustion-based power generation systems. These technologies contribute to better operational safety and higher energy-transition efficiency. Meanwhile, it places stringent requirements on instruments for fast, accurate and online monitoring of the system's thermochemical parameters, such as temperature and gas concentrations. For example: the flue gas temperature and

species concentrations were dynamically monitored to ensure the close-loop stability and combustion efficiency of a coal-fired power plant [6, 7]. Emissions of Nitrogen oxides (NO_x) were monitored online for efficient pollution controlling of solid waste incinerators [8, 9]. Exhaust gas temperature and species concentrations of gas turbine engines were measured to infer the combustion efficiency and operational safety [10-12]. However, such high-fidelity measurements are very challenging in harsh industrial environments due to the existence of significant distortion, such as the environmental noise and mechanical vibration.

Laser absorption spectroscopy (LAS), as a non-intrusive optical sensing technique [13], has been widely employed for *in situ* diagnosis of thermochemical parameters in industrial processes. It is implemented by scanning the laser wavelength across the absorbing transitions of target molecules and usually coincided with high-frequency wavelength modulation for better noise immunity. Traditionally, the demodulated absorption spectra from the laser transmission signal are fitted to the spectroscopic model through a least-square procedure [14]. The fitting process, however, is iterative and time/resource-consuming, hindering the real-time extraction of dynamically varying parameters. In response to this challenge, data-driven methods have become popular for rapid LAS-based gas monitoring, exploiting their remarkable computational efficiency in extracting spectral features.

The state-of-the-art data-driven LAS techniques [15-25] mainly utilize supervised-learning neural networks in an end-to-end manner, requiring a labelled dataset for training. Many of these models are trained solely on existing spectral databases, e.g., HITRAN [26], and directly learn the mapping between the absorbing spectra and the gaseous parameters. Some attempts constructed the training set using pure simulated spectra [15, 17, 23-25]. To adapt the models to incorporate measurement noise, recent works have either added synthetic noise to the simulated dataset [20] or combined limited experimental data with the simulated data [16]. These models favor simplicity, as the training set can be easily generated

Manuscript received xx; revised xx; accepted xx. This work was supported by the U.K. Engineering and Physical Sciences Research Council (EPSRC) Programme Grant LITECS under Grant EP/T012595/1. (Corresponding author: Chang Liu.)

Jiangnan Xia, Rui Zhang, Hugh McCann and Chang Liu are with the School of Engineering, The University of Edinburgh, EH9 3JL Edinburgh, U.K. (e-mail: C.Liu@ed.ac.uk).

Ihab Ahmed and Mohamed Pourkashanian are with the Department of Mechanical Engineering, The University of Sheffield, S10 2TN Sheffield, U.K.

Ian Armstrong, Michael Lengden, and Walter Johnstone are with the Department of Electronic and Electrical Engineering, University of Strathclyde, G1 1XQ Glasgow, U.K.

Color versions of one or more of the figures in this article are available online at <http://ieeexplore.ieee.org>

according to an estimated range of spectral parameters. However, their end-to-end nature can barely interpret spectral attributes that are physically linked to the gaseous parameters, and therefore, less adaptable for industrial scenarios where the *in situ* spectroscopic features cannot be estimated accurately.

To further improve model's performance, spectroscopic information of LAS, such as lineshape [19] and peak absorbance [22], is incorporated into the network training. Since spectral information imposes physical constraints on the neural network, it effectively enhances the applicability of data-driven LAS models in various measurement scenarios as well as their noise resistance. To date, this kind of physical-motivated models have been applied to denoise the measured spectra [21] and decouple the target absorption feature from its wavelength-neighbouring interferences [18]. However, they still require high-fidelity training labels and exhibit inadequate experimental spectra recovery. Recently, a hybrid LAS dataset was proposed by combining simulated labels and a portion of *in situ* experimental data labelled through the above-mentioned least-square fitting [27]. Although this method improves the recovery of *in situ* measured spectra, its dependence on fitting of post-experiment data hinders real-time combustion monitoring. In addition, with the reliance on labelled training set and less incorporation with the *in situ* spectral features, the above supervised models exhibit growing neural network complexity in order to achieve better generalization, and therefore, they are less deployable in industrial systems, such as on edge-computing devices

To address these limitations, a spectroscopy-constraint LAS network is proposed for fast extraction of thermochemical parameters from the modulated LAS signal in combustion-based power-generation systems. The main novelties of this paper are:

1) The spectroscopic constraint is imposed through the proposed autoencoder-structured neural network, making its training process exclusive on LAS measurement data from real industrial experiments. Incorporation of the spectroscopic model also enhances the robustness and generalizability of the proposed network for many industrial measurements.

2) The SC-LAS network is free from labelling experimental data. Such a label-free scheme eliminates complex signal post-processing of the experimental spectra, offering a new online solution for dynamic monitoring of thermochemical parameters using data-driven LAS.

3) The proposed network is constructed using a high-efficiency structure with fewer parameters, compared to the existing models. The inference speed of this network is significantly faster for real-time gas monitoring and is easy to be deployed on edge-computing units.

4) The SC-LAS model is tested on measuring the temperature and species concentration of the exhaust from a commercial aircraft engine, inferring its effectiveness in industrially relevant conditions.

The rest of the paper is organized as follows. In Section II, the preliminaries LAS are introduced. The architecture of the proposed network is described in Section III. Section IV

presents a case study on applying the proposed technique to a gas turbine engine. The paper is concluded in Section V.

II. PROBLEM FORMULATION AND PRELIMINARIES

Wavelength modulation spectroscopy (WMS) is a typical implementation of LAS that enables strong sensitivity and noise immunity in harsh environment [13]. It is carried out by superimposing a high-frequency sinusoidal modulation f_m [Hz] on the low-frequency current scan f_s [Hz] injected into the laser diode. Thus, the time-varying frequency of the light emitted by the laser (expressed here as wavenumber), $\nu(t)$, can be expressed as:

$$\nu(t) = \bar{\nu}_0 + a_s \cdot \cos(2\pi f_s t) + a_m \cdot \cos(2\pi f_m t) \quad (1)$$

where t is time, $\bar{\nu}_0$ [cm^{-1}] is the laser central wavenumber, and a_s and a_m are the amplitudes of the wavelength scan and modulation, respectively. Accompanied by the wavelength modulation, the incident laser intensity is also modulated and can be written as:

$$I_0(t) = \bar{I}_0 + i_s \cdot \cos(2\pi f_s t + \varphi_{\text{IM}}) + i_m \cdot \cos(2\pi f_m t + \varphi_{\text{FM}}) \quad (2)$$

where \bar{I}_0 is the averaged laser intensity, i_s and i_m are the amplitudes of intensity scan and modulation, respectively, and φ_{IM} and φ_{FM} are the phase differences between the laser intensity modulation (IM) and frequency modulation (FM), respectively.

The incident laser beam penetrates the target absorbing gas. According to the Beer-Lambert law [13], the transmitted laser intensity $I_t(t)$ is modelled as:

$$I_t(t) = I_0(t) \cdot \exp(-\alpha(\nu(t))) \quad (3)$$

$$\alpha(\nu(t)) = \phi_\nu(\nu(t)) \cdot P \cdot S_\nu(T) \cdot X \cdot L \quad (4)$$

where $\alpha(\nu(t))$ is the spectral absorbance which is parameterized by target flow parameters, i.e., pressure P [atm], temperature T [K], temperature-dependent line strength $S_\nu(T)$ [$\text{cm}^2 \text{atm}^{-1}$], target gas mole fraction X and line-of-sight absorption path length L [cm], as well as the transition lineshape profile $\phi_\nu(\nu(t))$.

In general, the first- and second-order harmonics of $I_t(t)$, noted respectively as $1f$ and $2f$, are demodulated by a digital quadrature lock-in amplifier at the frequencies of f_m and $2f_m$ [28, 29]. The calibration-free WMS signal can then be realized by calculating the $1f$ -normalized $2f$ spectrum (WMS- $2f/1f$) [30] as follows:

$$\Gamma(t) = \sqrt{\left[\left(\frac{X_{2f}}{R_{1f}} \right)_{\text{raw}} - \left(\frac{X_{2f}}{R_{1f}} \right)_{\text{bg}} \right]^2 - \left[\left(\frac{Y_{2f}}{R_{1f}} \right)_{\text{raw}} - \left(\frac{Y_{2f}}{R_{1f}} \right)_{\text{bg}} \right]^2} \quad (5)$$

where X_{nf} and Y_{nf} refer to the demodulated in-phase and quadrature nf ($n = 1$ or 2) components, $R_{1f} = \sqrt{X_{1f}^2 + Y_{1f}^2}$ is the magnitude of the first harmonic, and the subscripts $(\cdot)_{\text{raw}}$ and $(\cdot)_{\text{bg}}$ refer to the signal collected in the scenarios with and without the absorption, respectively.

According to above discussion, the spectra $\Gamma(t)$ can be expressed as a forward function, which is constrained with the absorption spectroscopic model and parameterized by the laser

characteristics, i.e., $v(t)$ and $I_0(t)$, and the flow parameters T , X , P and L . In addition, $\Gamma(t)$ can also be affected by the flow-related line-shift μ [cm^{-1}] of $v(t)$, which will be discussed in detail in Section III. We denote the forward function as $f(\cdot)$ to express $\Gamma(t)$ as:

$$\Gamma(t) = f(T, X, P, L, v(t) + \mu, I_0(t)) \quad (6)$$

However, solving the inverse function $f^{-1}(\cdot)$ of (6) to infer T , X , P from the measured $\Gamma(t)$ is complex. Although $v(t)$ and $I_0(t)$ are pre-determined before the experiment, non-linearity exists in both $S_v(T)$ in (4) and $\Gamma(t)$ in (5), resulting in non-existence of analytic solutions for $f^{-1}(\cdot)$. Spectral fitting methods have been adopted by iteratively updating the flow parameters to calculate the theoretical $\Gamma(t)$ using (6) and then to least-square fit to the measured one [14]. Although it exhibits high accuracy, fitting of a single absorption spectrum is time-consuming, which takes over a second per laser scan even using modern high-level processors. The slow response limits the online performance of WMS and thus its application to active combustion control. To accelerate solution of the non-linear $f^{-1}(\cdot)$, we design a neural network, as detailed in the next section, to replace the spectral fitting method.

III. MODEL ESTABLISHMENT

As shown in Fig. 1, the SC-LAS model is designed using an autoencoder (AE) structured neural network. The proposed network is completely free from synthetic labels, thus being superior to any of the existing data-driven LAS models in terms of generalizability to various test cases. Spectroscopic constraint is integrated in this encoder-decoder structured network, enabling its training to be solely dependent on $\Gamma(t)$ measured under industrial conditions.

A. Dual-branch encoder

Ratio thermometry [31] using two laser lines selected at wavenumbers ν_1 and ν_2 with different line strengths $S_v(T)$, has been widely adopted for simultaneous temperature and gas concentration retrieval. The two measured spectral vectors with l wavenumber samples, noted as $\Gamma_{\nu_1} \in \mathbb{R}^{l \times 1}$ and $\Gamma_{\nu_2} \in \mathbb{R}^{l \times 1}$, are firstly concatenated as the input vector $\Gamma \in \mathbb{R}^{l \times 2}$ for the dual-branch encoder. The encoder consists of a spectral feature extractor, a dual-branch temperature and concentration predictor and a line-shift estimator.

1) Spectral feature extractor

The spectral feature extractor is constructed using a one-dimensional convolutional neural network (1D-CNN). Because of its compact structure with low computational complexity [32], 1D-CNN is well-suited to real-time and low-cost 1D signal processing in our application. As shown in Fig. 2, the spectral feature maps are extracted by three 1D convolutional layers, i.e., Conv1, Conv2 and Conv3. The 1D-CNN layers learn the hierarchies from the spectral sequences and the correlation between the two transitions. The forward propagation of the 1D-CNN is formulated as:

$$\mathbf{O}_{\text{Conv1}} = \sigma_{\text{ReLU}}(\mathbf{W}_{\text{Conv1}} * \Gamma + \mathbf{b}_{\text{Conv1}}) \quad (7)$$

$$\mathbf{O}_{\text{Conv2}} = \sigma_{\text{ReLU}}(\mathbf{W}_{\text{Conv2}} * \mathbf{O}_{\text{Conv1}} + \mathbf{b}_{\text{Conv2}}) \quad (8)$$

$$\mathbf{O}_{\text{Conv3}} = \sigma_{\text{ReLU}}(\mathbf{W}_{\text{Conv3}} * \mathbf{O}_{\text{Conv2}} + \mathbf{b}_{\text{Conv3}}) \quad (9)$$

where $*$ represents the 1D convolution operand, $\sigma_{\text{ReLU}}(\cdot)$ is the ReLU activation function, and $\mathbf{O}_{\text{Conv1}} \in \mathbb{R}^{H_{O1} \times C_{O1}}$, $\mathbf{O}_{\text{Conv2}} \in \mathbb{R}^{H_{O2} \times C_{O2}}$ and $\mathbf{O}_{\text{Conv3}} \in \mathbb{R}^{H_{O3} \times C_{O3}}$ are output spectral feature maps for each 1D-CNN layer, respectively. The dimensional parameters, H_{O1} , H_{O2} and H_{O3} , are the output lengths for the three layers, while C_{O1} , C_{O2} and C_{O3} are the numbers of output channels. $\mathbf{W}_{\text{Conv1}} \in \mathbb{R}^{H_{W1} \times C_{W1}}$ ($\mathbf{W}_{\text{Conv2}} \in \mathbb{R}^{H_{W2} \times C_{W2}}$ and $\mathbf{W}_{\text{Conv3}} \in \mathbb{R}^{H_{W3} \times C_{W3}}$) and $\mathbf{b}_{\text{Conv1}} \in \mathbb{R}^{1 \times C_{O1}}$ ($\mathbf{b}_{\text{Conv2}} \in \mathbb{R}^{1 \times C_{O2}}$ and $\mathbf{b}_{\text{Conv3}} \in \mathbb{R}^{1 \times C_{O3}}$) are the 1D convolution kernel and the bias vector from layer Conv1 (Conv2 and Conv3), respectively. Dimensional parameters H_{W1} (H_{W2} and H_{W3}) and C_{W1} (C_{W2} and C_{W3}) are the kernel lengths and the numbers of kernel channels for layer Conv1 (Conv2 and Conv3), respectively.

2) Dual-branch temperature and concentration predictor

Temperature and gas concentration are predicted in this stage from the extracted spectral feature $\mathbf{O}_{\text{Conv3}}$. As shown in Fig. 2, $\mathbf{O}_{\text{Conv3}}$ is firstly flattened and refined through a fully-connected (FC) layer:

$$\mathbf{Z} = \sigma_{\text{ReLU}}(\mathbf{W}_{\text{FC}} \cdot F(\mathbf{O}_{\text{Conv3}}) + \mathbf{b}_{\text{FC}}) \quad (10)$$

where $F(\cdot)$ represents the flattening transformation. $\mathbf{Z} \in \mathbb{R}^{H_Z \times 1}$ is the flattened and refined feature vector with length of H_Z . $\mathbf{W}_{\text{FC}} \in \mathbb{R}^{H_Z \times (H_{O3} \cdot C_{O3})}$ and $\mathbf{b}_{\text{FC}} \in \mathbb{R}^{H_Z \times 1}$ are the weight and bias parameters of the FC layer, respectively.

The refined feature vector \mathbf{Z} is fed into a sub-network with two branches to predict temperature and concentration. Within each branch, four layers constructed by multi-layer perceptron

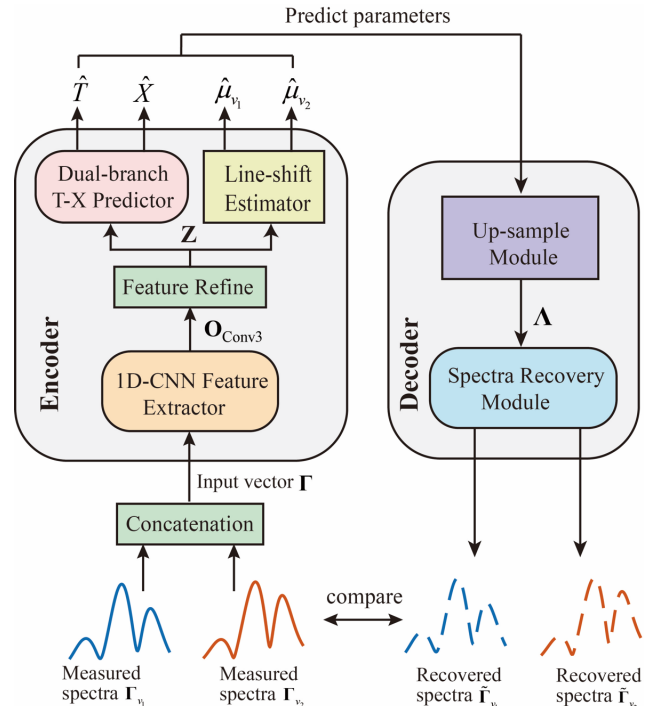


Fig. 1 Overall architecture of the proposed SC-LAS neural network.

(MLP) are established. In industrial combustion processes, temperature and post-combustion water vapor (H₂O) concentration are positively correlated when using either hydrocarbon or carbon-free fuels, such as hydrogen and ammonia in the latter case. In general, higher temperature indicates stronger chemical reactions and thus higher H₂O concentration. Therefore, an internal crosstalk is incorporated between two branches to represent this correlation. The forward propagation for the dual-branch predictor is formulated as:

$$\boldsymbol{\tau}_k = \begin{cases} \sigma_{\text{PreLU}}(\mathbf{W}_k^r \cdot \mathbf{Z} + \mathbf{C}_k^z \odot (\mathbf{W}_k^z \cdot \mathbf{Z})), k=1 \\ \sigma_{\text{PreLU}}(\mathbf{W}_k^r \cdot \boldsymbol{\tau}_{k-1} + \mathbf{C}_k^z \odot (\mathbf{W}_k^z \cdot \boldsymbol{\chi}_{k-1})), k=2,3 \\ \sigma_{\text{Tanh}}(\mathbf{W}_k^r \cdot \boldsymbol{\tau}_{k-1} + \mathbf{C}_k^z \odot (\mathbf{W}_k^z \cdot \boldsymbol{\chi}_{k-1})), k=4 \end{cases} \quad (11)$$

$$\boldsymbol{\chi}_k = \begin{cases} \sigma_{\text{PreLU}}(\mathbf{W}_k^z \cdot \mathbf{Z} + \mathbf{C}_k^r \odot (\mathbf{W}_k^r \cdot \mathbf{Z})), k=1 \\ \sigma_{\text{PreLU}}(\mathbf{W}_k^z \cdot \boldsymbol{\chi}_{k-1} + \mathbf{C}_k^r \odot (\mathbf{W}_k^r \cdot \boldsymbol{\tau}_{k-1})), k=2,3 \\ \sigma_{\text{Tanh}}(\mathbf{W}_k^z \cdot \boldsymbol{\chi}_{k-1} + \mathbf{C}_k^r \odot (\mathbf{W}_k^r \cdot \boldsymbol{\tau}_{k-1})), k=4 \end{cases} \quad (12)$$

where $k \in \{1, 2, 3, 4\}$ is the index of each layer in the dual-branch predictor; $\mathbf{W}_k^r \in \mathbb{R}^{N_{k+1} \times N_k}$ ($\mathbf{W}_k^z \in \mathbb{R}^{N_{k+1} \times N_k}$) is the k^{th} MLP layer weight from temperature (concentration) branch; and $\boldsymbol{\tau}_k \in \mathbb{R}^{N_k \times 1}$ and $\boldsymbol{\chi}_k \in \mathbb{R}^{N_k \times 1}$ are the corresponding output vectors from the temperature and concentration branches,

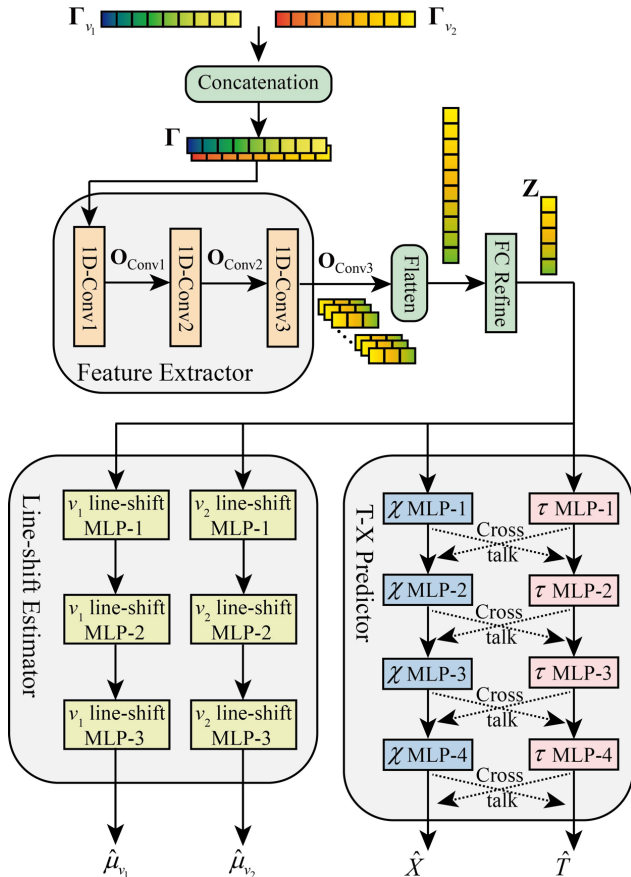


Fig. 2 Architecture of the dual-branch encoder in the SC-LAS

respectively. The trainable parameters $\mathbf{C}_k^r \in \mathbb{R}^{N_k \times 1}$ and $\mathbf{C}_k^z \in \mathbb{R}^{N_k \times 1}$ are the k^{th} MLP layer crosstalk weights that add correlation between temperature and concentration branches. Symbol \odot denotes the element-wise production. $\sigma_{\text{Tanh}}(\cdot)$ is the Tanh activation function to normalize the predicted temperature and concentration scale, $\hat{T} = \boldsymbol{\tau}_4 \in \mathbb{R}^{1 \times 1}$ and $\hat{X} = \boldsymbol{\chi}_4 \in \mathbb{R}^{1 \times 1}$, distributed between -1 and 1.

3) Line-shift estimator

The laser transition line centre $\bar{\nu}_0$ in (1) is affected by the flow velocity along the laser propagation direction and will exhibit the Doppler shift. Due to the wavenumber-scanning nature, this line shift in laser wavelength is translated into a shift of the measured spectra $\Gamma(t)$ on the time t axis. Thus, estimators to compensate this line shift μ for each of the two transitions are established in this sub-network.

The line-shift estimator is constructed by a 3-layer MLP network for each transition and has a similar structure to the dual-branch predictor but without the cross-talk structure. It takes the refined feature vector \mathbf{Z} as input and outputs the estimated line shift:

$$\hat{\mu}_{v_1} = \sigma_{\text{Tanh}}(\mathbf{W}_3^{v_1} \cdot \sigma_{\text{PreLU}}(\mathbf{W}_2^{v_1} \cdot \sigma_{\text{PreLU}}(\mathbf{W}_1^{v_1} \cdot \mathbf{Z}))) \quad (13)$$

$$\hat{\mu}_{v_2} = \sigma_{\text{Tanh}}(\mathbf{W}_3^{v_2} \cdot \sigma_{\text{PreLU}}(\mathbf{W}_2^{v_2} \cdot \sigma_{\text{PreLU}}(\mathbf{W}_1^{v_2} \cdot \mathbf{Z}))) \quad (14)$$

where $\mathbf{W}_1^{v_1} \in \mathbb{R}^{M_1 \times H_Z}$, $\mathbf{W}_2^{v_1} \in \mathbb{R}^{M_2 \times M_1}$ and $\mathbf{W}_3^{v_1} \in \mathbb{R}^{M_3 \times M_2}$ ($\mathbf{W}_1^{v_2} \in \mathbb{R}^{M_1 \times H_Z}$, $\mathbf{W}_2^{v_2} \in \mathbb{R}^{M_2 \times M_1}$ and $\mathbf{W}_3^{v_2} \in \mathbb{R}^{M_3 \times M_2}$) are the weight of first (second and third) MLP layer for transition v_1 (v_2). $\hat{\mu}_{v_1}$ and $\hat{\mu}_{v_2}$ are the output line-shift scalars normalized between -1 and 1 for transition line v_1 and v_2 , respectively.

B. Spectral Decoder

The decoder established in this stage is the reverse process of the encoder, i.e., recovering the spectra of the transitions v_1 and v_2 from the \hat{T} and \hat{X} as well as the line shifts $\hat{\mu}_{v_1}$ and $\hat{\mu}_{v_2}$ estimated by the encoder. In other words, it can represent the spectroscopic model in (6). By comparing the recovered spectra with the measurements, absorption spectroscopic model is imposed as physical constraint on the network.

As shown in Fig. 3, the decoder contains an up-sampling module using MLP and a spectra recovery module based on the transposed 1D-CNN. The up-sampling expands the dimension of four encoder-estimated scalar inputs, i.e., $(\hat{T}, \hat{X}, \hat{\mu}_{v_1}, \hat{\mu}_{v_2})$, using two-layer MLPs:

$$\mathbf{U}_T = \sigma_{\text{PreLU}}(\mathbf{W}_{U_2}^T \cdot \sigma_{\text{PreLU}}(\mathbf{W}_{U_1}^T \cdot \hat{T})) \quad (15)$$

$$\mathbf{U}_X = \sigma_{\text{PreLU}}(\mathbf{W}_{U_2}^X \cdot \sigma_{\text{PreLU}}(\mathbf{W}_{U_1}^X \cdot \hat{X})) \quad (16)$$

$$\mathbf{U}_{\mu_{v_1}} = \sigma_{\text{PreLU}}(\mathbf{W}_{U_2}^{\mu_{v_1}} \cdot \sigma_{\text{PreLU}}(\mathbf{W}_{U_1}^{\mu_{v_1}} \cdot \hat{\mu}_{v_1})) \quad (17)$$

$$\mathbf{U}_{\mu_{v_2}} = \sigma_{\text{PreLU}}(\mathbf{W}_{U_2}^{\mu_{v_2}} \cdot \sigma_{\text{PreLU}}(\mathbf{W}_{U_1}^{\mu_{v_2}} \cdot \hat{\mu}_{v_2})) \quad (18)$$

where $\mathbf{W}_{U_1}^T \in \mathbb{R}^{H_{U_1} \times 1}$ ($\mathbf{W}_{U_2}^T \in \mathbb{R}^{H_{U_2} \times H_{U_1}}$), $\mathbf{W}_{U_1}^X \in \mathbb{R}^{H_{U_1} \times 1}$ ($\mathbf{W}_{U_2}^X \in \mathbb{R}^{H_{U_2} \times H_{U_1}}$), $\mathbf{W}_{U_1}^{\mu_{v_1}} \in \mathbb{R}^{H_{U_1} \times 1}$ ($\mathbf{W}_{U_2}^{\mu_{v_1}} \in \mathbb{R}^{H_{U_2} \times H_{U_1}}$) and $\mathbf{W}_{U_2}^{\mu_{v_2}} \in \mathbb{R}^{H_{U_2} \times 1}$ ($\mathbf{W}_{U_2}^{\mu_{v_2}} \in \mathbb{R}^{H_{U_2} \times H_{U_1}}$) are the weights from first

(second) up-sampling layer for \hat{T} , \hat{X} , $\hat{\mu}_{v_1}$ and $\hat{\mu}_{v_2}$, respectively. The up-sampled input vectors \mathbf{U}_T , \mathbf{U}_X , $\mathbf{U}_{\mu_{v_1}}$ and $\mathbf{U}_{\mu_{v_2}}$ with length H_{U_2} are concatenated, and then fused by a fully-connected layer:

$$\mathbf{A} = R(\sigma_{\text{PReLU}}(\mathbf{W}_{\text{Fuse}} \cdot \text{cat}(\mathbf{U}_T, \mathbf{U}_X, \mathbf{U}_{\mu_{v_1}}, \mathbf{U}_{\mu_{v_2}}))) \quad (19)$$

where $\mathbf{W}_{\text{Fuse}} \in \mathbb{R}^{(4 \times H_{U_2}) \times (4 \times H_{U_2})}$ is the weight of the fusion FC-layer, $\text{cat}(\cdot)$ represents the concatenation operation, and $R(\cdot)$ reshapes the output vector to $\mathbf{A} \in \mathbb{R}^{H_{U_2} \times 4}$.

Then, the up-sampled vector \mathbf{A} passes a 3-layer transposed 1D-CNN and a FC layer for spectral recovery of the two transitions. We denote $\tilde{h}_i(\cdot)$ as the i^{th} ($i = 1, 2, 3$) transposed 1D convolutional layer using the PReLU activation function. The final transposed 1D convolution output $\tilde{\mathbf{I}} \in \mathbb{R}^{2 \times H_{\tilde{I}}}$ is expressed as:

$$\tilde{\mathbf{I}} = \tilde{h}_3(\tilde{h}_2(\tilde{h}_1(\mathbf{A}))) \quad (20)$$

Finally, the spectra for v_1 and v_2 are recovered through two separate FC layers:

$$\tilde{\Gamma}_{v_1} = \sigma_{\text{PReLU}}(\mathbf{W}_{\text{rec}}^{v_1} \cdot \tilde{\mathbf{I}}[1,:]) \quad (21)$$

$$\tilde{\Gamma}_{v_2} = \sigma_{\text{PReLU}}(\mathbf{W}_{\text{rec}}^{v_2} \cdot \tilde{\mathbf{I}}[2,:]) \quad (22)$$

where $[1, :]$ and $[2, :]$ are the first- and second-channel slice operations, respectively, and $\mathbf{W}_{\text{rec}}^{v_1} \in \mathbb{R}^{l \times H_{\tilde{I}}}$ and $\mathbf{W}_{\text{rec}}^{v_2} \in \mathbb{R}^{l \times H_{\tilde{I}}}$ are the weights of the FC layers for spectra recovery of the transitions v_1 and v_2 . The resulting $\tilde{\Gamma}_{v_1} \in \mathbb{R}^{l \times 1}$ and $\tilde{\Gamma}_{v_2} \in \mathbb{R}^{l \times 1}$ are the recovered spectra of the two transitions, which will be compared to the measured spectra, Γ_{v_1} and Γ_{v_2} , for the encoder training. The training process of the proposed network is

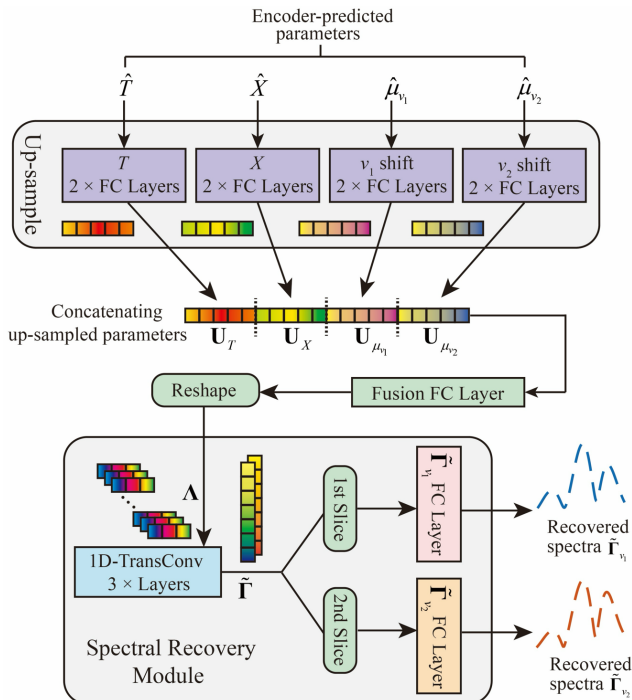


Fig. 3 Architecture of the spectral decoder in the SC-LAS.

illustrated in the case study in the next section.

IV. CASE STUDY: AIRCRAFT ENGINE EXHAUST MONITORING

A case study is carried out in this section by using the proposed SC-LAS model to measure temperature and H_2O concentration in the exhaust of a commercial aircraft auxiliary power unit (APU, Honeywell 131-9A) running on a test stand at the University of Sheffield. The APU is commonly situated at the tail of an aircraft, which supplies airflow and additional power to various systems, including the air conditioning and aircraft control systems.

A. System set up

Fig. 4 (a) shows the picture of the *in situ* APU set up and the deployment of the LAS sensor. An exhaust plume guide tube with a diameter of 24 cm and a length of 30 cm is attached to the APU exit, which directs the plume into the exhaust system. A K-type thermocouple is inserted at the inlet of the guide tube to provide a reference gas temperature measurement. The laser beam is positioned on a plane that is located 3 cm downstream from the outlet of the guide tube. Since the combustor exhaust velocity can reach up to 100 m/s, the exhaust temperature and concentration difference between the inlet and outlet of the guide tube is assumed to be negligible.

Fig. 4 (b) illustrates the schematic of the LAS measurement plane, viewing from the axial direction of the APU exhaust outlet. Specifically, two DFB laser diodes (NEL NLK1E5EAAA and NEL NLK1B5EAAA) with wavenumber centered at $v_1 = 7185.59 \text{ cm}^{-1}$ and $v_2 = 7444.36 \text{ cm}^{-1}$, are scanned at $f_s = 1 \text{ kHz}$ and modulated at $f_{m1} = 100 \text{ kHz}$ and $f_{m2} = 130 \text{ kHz}$, respectively. The selected two H_2O absorption transitions have been widely used in LAS experiments, which have good sensitivity within the temperature range 300-1500 K [14, 28] and H_2O concentration range 0-0.1, covering those in the target APU exhaust at various working conditions. These two lasers are frequency multiplexed [28] using a fiber coupler and

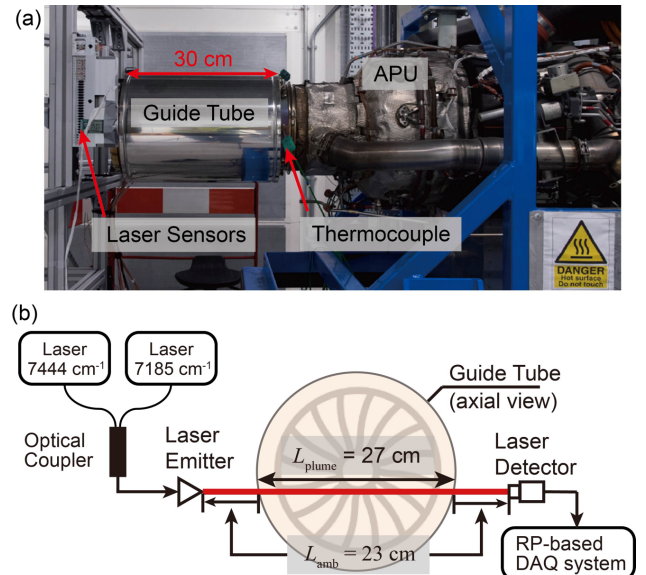


Fig. 4 (a) APU and LAS sensor setup. (b) Laser beam arrangement viewing from the axial direction of the APU exit.

collimated to penetrate the exhaust plume. The distance between the collimator and the photodetector (Hamamatsu, G12182-010K), i.e., the absorption path length L , is fixed at 50 cm, within which 27 cm of its length, denoted as L_{plume} , is located in the plume area while the length in ambient region L_{amb} is 23 cm.

The transmitted laser signal $I_i(t)$ is collected by a Red Pitaya (RP)-based DAQ system [29] which can provide 250 Hz temporal resolution with the quantization frequency f_q of 15.625 MHz. An online digital lock-in amplifier (DLIA) scheme [28] aided by a cascaded integrator-comb filter with decimation factor $D = 32$, is integrated into the DAQ system. As a result, there are 488 spectral wavenumber samples ($f_q/f_s/D$) within a laser scan. For each absorption transition, the central 120 samples of the downwards sinusoid semi-scan are selected to extract the exhaust parameters. Thus, the two input WMS-2/1f spectral vectors, i.e., $\mathbf{\Gamma}_{v_1}$ and $\mathbf{\Gamma}_{v_2}$, have a length l of 120.

B. Network training

1) Decoder pre-training

The implementation parameters for the spectral decoder are listed in TABLE I. It is notable that the two-layer MLPs in (15-18) for up-sampling the estimated \hat{T} , \hat{X} , $\hat{\mu}_{v_1}$ and $\hat{\mu}_{v_2}$, have the same structure and parameter dimensions. For simplicity, only one set of these parameters is listed.

Before the APU test, the decoder network should be pre-trained to sufficiently approximate the spectroscopic model described in (6) and it is independent on a specific industrial scene. Thus, the decoder pre-training spectral labels, i.e., $(\mathbf{\Gamma}_{v_1}^{\text{label}}, \mathbf{\Gamma}_{v_2}^{\text{label}})$ for v_1 and v_2 , can be generated directly by equation (6) giving an input set $(T, X, \mu_{v_1}, \mu_{v_2})$, without adding any noise. To cover conditions from the ambient environment to the common working load of APU engines [33], T ranges from $T_{\min} = 280$ K to $T_{\max} = 1673$ K with a step of 7 K, while X ranges from $X_{\min} = 0.002$ to $X_{\max} = 0.0816$ with a step of 0.0004, giving a total of 40,000 combinations. Then, μ_{v_1} and μ_{v_2} are generated using random values between $\mu_{\min} = -0.02$ cm⁻¹ and $\mu_{\max} = 0.02$ cm⁻¹. All the inputs are normalized within -1 and 1 for training, noted as $(\hat{T}, \hat{X}, \hat{\mu}_{v_1}, \hat{\mu}_{v_2})$. For example, the normalized temperature \hat{T} is calculated as:

$$\hat{T} = 2 * (T - T_{\min}) / (T_{\max} - T_{\min}) - 1 \quad (23)$$

Then, according to the system set up, P and L in (6) are fixed at 1 atm and 50 cm, respectively. $v(t)$ and $h(t)$ are obtained from the laser characterization.

Using the dataset generated above, i.e., $\{(\hat{T}, \hat{X}, \hat{\mu}_{v_1}, \hat{\mu}_{v_2}), (\mathbf{\Gamma}_{v_1}^{\text{label}}, \mathbf{\Gamma}_{v_2}^{\text{label}})\}$, the decoder is optimized by minimizing the difference between its output spectra and the label set. To make the full use of each point in the spectra, the normalized L1 loss function L_{dec} is used:

$$L_{\text{dec}} = \beta \frac{1}{l} \sum_i \frac{\|\mathbf{\Gamma}_{v_1}^{\text{label}} - \tilde{\mathbf{\Gamma}}_{v_1}\|}{\|\mathbf{\Gamma}_{v_1}^{\text{label}}\|} + (1 - \beta) \frac{1}{l} \sum_i \frac{\|\mathbf{\Gamma}_{v_2}^{\text{label}} - \tilde{\mathbf{\Gamma}}_{v_2}\|}{\|\mathbf{\Gamma}_{v_2}^{\text{label}}\|} \quad (24)$$

where $\tilde{\mathbf{\Gamma}}_{v_1}$ and $\tilde{\mathbf{\Gamma}}_{v_2}$ are the decoder output spectra for v_1 and v_2 , respectively, and β is 0.5 to balance the loss on the two transitions. The Adam optimizer [34] is adopted with the learning rate $\alpha_{\text{dec}} = 0.001$ and the batch size $B = 128$. The decoder training was conducted using the Pytorch framework on a desktop PC (AMD R7-5800x, 32 GB RAM, NVIDIA RTX 3060Ti). It is trained for 300 epochs until the loss L_{dec} is below 0.5%, indicating that the decoder can accurately represent the spectroscopic model expressed by (6).

2) Encoder Training

The encoder, performing the inverse function $f^{-1}(\cdot)$ of (6) for thermochemical parameter extraction, is trained exclusively on engine test measurement data with the decoder parameters frozen. The encoder implementation parameters are listed in TABLE II. Giving the same dimensions, only one set parameters of the 4-layer MLPs in the T-X predictor and the 3-layer MLPs in the line-shift estimator are listed for simplicity. We randomly selected $N_{\text{enc}} = 20,000$ measured spectral vectors $(\mathbf{\Gamma}_{v_1}, \mathbf{\Gamma}_{v_2})$ among the total 87,500 frames during the whole APU running.

The encoder takes $(\mathbf{\Gamma}_{v_1}, \mathbf{\Gamma}_{v_2})$ as inputs and estimates the normalized temperature, concentration and line shifts, $(\hat{T}, \hat{X}, \hat{\mu}_{v_1}, \hat{\mu}_{v_2})$, which are fed into the fixed decoder to recover the spectra. The encoder network is then optimized by

TABLE I. DECODER IMPLEMENTATION PARAMETERS

Up-sampling Module				
	Input	Weight size	Output	
up-sampling FC 1	1	(1, 32)	32	
up-sampling FC 2	32	(32, 64)	64	
Fusion FC	256	(256, 256)	256	
Spectral Recovery Module				
	Input	Kernel	Stride	Output
TransConv1	(64, 4)	3	3	(16, 12)
TransConv2	(16, 12)	3	3	(8, 36)
TransConv3	(8, 36)	3	3	(2, 108)
	Input	Weight size	Output	
$\tilde{\mathbf{\Gamma}}_{v_1}$ FC	108	(108, 120)	120	
$\tilde{\mathbf{\Gamma}}_{v_2}$ FC	108	(108, 120)	120	

TABLE II. ENCODER IMPLEMENTATION PARAMETERS

Feature Extractor				
	Input	Kernel	Stride	Output
1D-Conv1	(2, 120)	3	3	(8, 40)
1D-Conv2	(8, 40)	3	3	(16, 13)
1D-Conv3	(16, 13)	3	3	(64, 4)
T-X Predictor				
	Input	Weight size	Output	
Refine FC	256	(256, 128)	128	
Predictor FC1	128	(128, 64)	64	
Predictor FC2	64	(64, 32)	32	
Predictor FC3	32	(32, 16)	16	
Predictor FC4	16	(16, 1)	1	
Line Shift Estimator				
	Input	Weight size	Output	
Line shift FC1	128	(128, 64)	64	
Line shift FC2	64	(64, 32)	32	
Line shift FC3	32	(32, 1)	1	

minimizing the difference between the decoder recovered and measured spectra. Since the well-trained decoder can sufficiently represent the spectroscopic model in (6), the constraint is imposed during training. The L1 loss function is selected as:

$$L_{\text{enc}} = \gamma \frac{1}{l} \cdot \sum_l \|\Gamma_{v_1} - \tilde{\Gamma}_{v_1}\| + (1-\gamma) \frac{1}{l} \cdot \sum_l \|\Gamma_{v_2} - \tilde{\Gamma}_{v_2}\| \quad (25)$$

$$(\tilde{\Gamma}_{v_1}, \tilde{\Gamma}_{v_2}) = \text{dec}[\hat{T}, \hat{X}, \hat{\mu}_{v_1}, \hat{\mu}_{v_2}] \quad (26)$$

where γ is the spectral weight hyper-parameter for the two transitions. $\text{dec}[\cdot]$ represents the well-trained decoder network, performing the forward function $f(\cdot)$ to recover the spectra vectors $(\tilde{\Gamma}_{v_1}, \tilde{\Gamma}_{v_2})$.

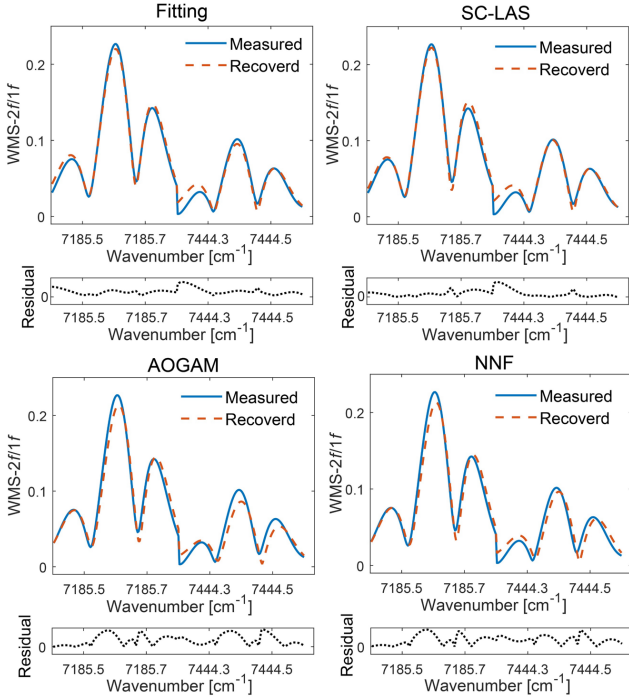


Fig. 5 Comparison of the measured WMS-2f/1f signal and its spectra recovery using (a) spectra fitting (b) SC-LAS (c) NNF and (d) AOGAM.

The Adam optimizer with $\gamma=0.7$ and $B=128$ is used for the encoder training. The learning rate α_{enc} is decaying with the epoch number n exponentially as $\alpha_{\text{enc}} = 0.001 \times 0.99^n$. The optimization of encoder was conducted on the same device with the decoder training for 300 epochs.

C. Test result and discussion

During the APU test, the engine experienced different working conditions, including ignition, acceleration, no-load and full-load states, which indicates a highly dynamic *in situ* test environment. Under these working conditions, its plume temperature and exhausts H_2O concentration are valuable for control optimization and emission evaluation. To highlight the advantages of the proposed SC-LAS model, two network-based models for gas parameters extraction from LAS signal, i.e., the neural network filter (NNF) in [20] and the adaptively optimized gas analysis model (AOGAM) in [21], are adopted for performance comparison, including the estimation accuracy and computational efficiency. These two models are typical representatives of methods trained solely on synthetic data and with constraint of measured spectra, respectively. In addition, the traditional method, i.e., spectral fitting, is used as the accuracy benchmark.

1) Evaluation of estimation accuracy

The model estimation accuracy is evaluated from two aspects: (a) WMS-2f/1f spectra recovery and (b) temperature and H_2O concentration retrieval. Fig. 5 shows Γ sampled from the APU test and its recovery using the spectral fitting benchmark, the SC-LAS, NNF and AOGAM. The residual is calculated as the difference between the measured $(\Gamma_{v_1}, \Gamma_{v_2})$ and the recovered $(\tilde{\Gamma}_{v_1}, \tilde{\Gamma}_{v_2})$. The proposed SC-LAS model has a similar performance of spectral recovery compared to the benchmark, indicating well-covered spectral features as spectroscopic constraint is imposed on these two methods. In contrast, larger mismatch is observed for the NNF and AOGAM around the peak absorbance at wavenumbers close to 7185.6 cm^{-1} and 7444.4 cm^{-1} .

To further quantitatively evaluate the spectral recovery, the mean relative curve error (RCE) and absolute curve error (ACE) are introduced as metrics. The RCE and ACE for the transition v is defined as:

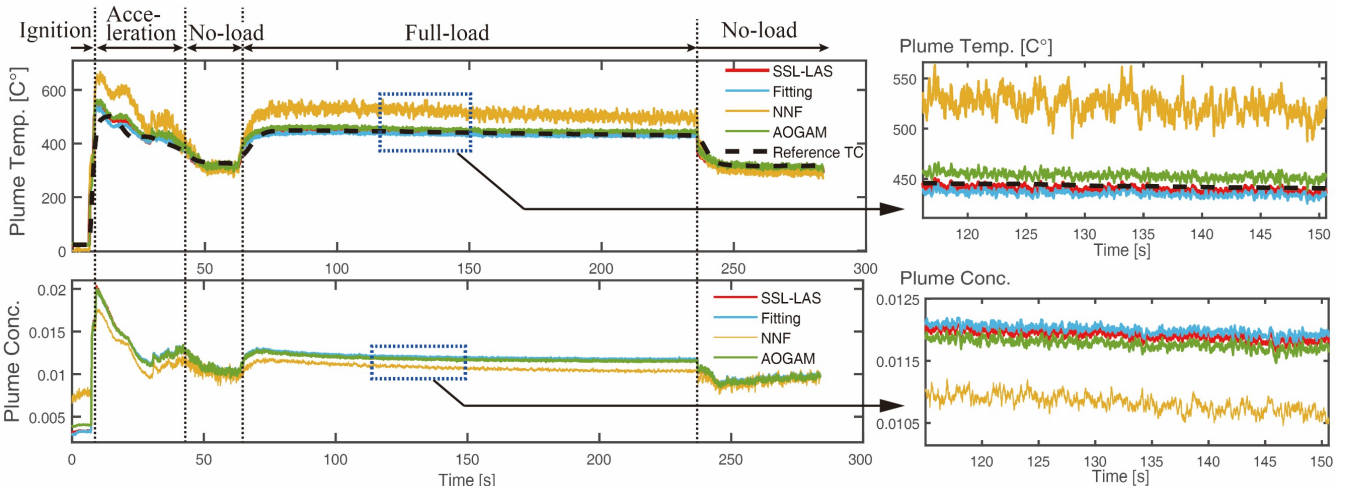


Fig. 6 Comparison of the APU plume temperature and H_2O concentration obtained by SC-LAS, spectral fitting, AOGAM and NNF.

$$\text{RCE}_v = (1/l) \sum_i \frac{\|\Gamma_v - \tilde{\Gamma}_v\|}{\|\Gamma_v\|} \quad (27)$$

$$\text{ACE}_v = (1/l) \sum_i \|\Gamma_v - \tilde{\Gamma}_v\| \quad (28)$$

where the subscript v represents either of the transitions.

As listed in TABLE III, for either of the two transitions, the proposed SC-LAS gives the closest RCE and ACE values compared to the fitting benchmark. It outperforms the NNF and AOGAM by lowering the RCE by, respectively, 31.5 % and 24.6 %, and lowering the ACE by, respectively, 50.3 % and 33.9 %.

In Fig. 6, the plume temperature and H₂O concentration inferred from the proposed SC-LAS model as well as the spectral fitting, AOGAM and NNF models are shown. The measurement from the thermocouple (TC) with 10 Hz temporal resolution is also displayed as the referenced plume temperature. Compared to the TC reference, the 250 Hz temporal resolution of the LAS technique reveals more dynamic details during the APU engine run. For example, a much sharper increase both in temperature and H₂O concentration are observed after 6 s, indicating the fuel is ignited in the APU. Due to the effect of heat aggregation on the TC, the peak plume temperature at 8 s measured by TC reference is lower than that estimated by any of the spectral fitting, SC-LAS, AOGAM and NNF.

To further evaluate the accuracy of each method, we compare the temperature and H₂O concentration under the full-load condition of APU. In this period, the TC measurement can be regarded as a relatively convincing reference as the relatively stabilized temperature mitigates the influence from the slow-response sensing nature. Measurement results between 110 s and 150 s of the APU operation is zoomed in and shown in the subplot of Fig. 6. The stand deviation (std) during that period is

TABLE III. RCEs and ACEs of WMS-2F/1F SPECTRA RECOVERY and FLOW PARAMETERS STD USING SPECTRAL FITTING, SC-LAS, NNF AND AOGAM.

		Fitting	SC-LAS	NNF	AOGAM
7185 cm ⁻¹	RCE	0.0686	0.0700	0.0971	0.0864
	ACE	0.0129	0.0127	0.0190	0.0160
7444 cm ⁻¹	RCE	0.1872	0.1936	0.2471	0.2402
	ACE	0.0219	0.0210	0.0322	0.0295
Full-load T std		3.291	3.426	11.459	4.160
Full-load X std		9.24e-5	9.34e-5	1.51e-4	9.93e-5

TABLE IV. EVALUATION OF COMPUTATION EFFICIENCY FOR SPECTRAL FITTING, SC-LAS, NNF AND AOGAM.

	Fitting	SC-Encoder	NNF	AOGAM
Model parameters		0.32 MB	17.27 MB	39.53 MB
Train/epoch		1.69 s	26.65 s	312.34 s
Inference/scan	1.02 s	0.047 ms	0.29 ms	19.46 ms

TABLE V. EVALUATION of SC-LAS ENCODER DEPLOYMENT on a RASPBERRY PI 4B

CPU usage	RAM usage	Power consumption	Time per scan
12.61 %	0.55 %	1.51 W	0.091 ms

also listed in Table IV to reflect the robustness to noise. Consisted with the spectra recovery result, it illustrates that the spectral fitting and SC-LAS model exhibit more accurate temperature estimation, i.e., closer to the TC reference, with lower degree of fluctuations, compared to the AOGAM and NNF models. Since probe sampling is not available for real-time H₂O monitoring during the APU test, we use spectral-fitted H₂O concentration as the reference. As shown in the subplot of Fig. 6 (b), the proposed SC-LAS model gives closer estimation to the spectral-fitted H₂O concentration than the AOGAM and NNF models. It also exhibits the smallest std among the three network-based approaches.

The result above indicates the effectiveness of the explicit spectroscopic constraint in SC-LAS. The NNF model with simple MLPs structure, exhibits the worst result as its dependency on pure simulated dataset cannot handle the difference between the synthetic data and *in situ* APU test data. The AOGAM model gives a much better performance by adding a shape constraint of the measured spectra, but the lack of an inherent spectroscopic model makes its training still rely on synthetic dataset. On the contrary, in both SC-LAS and spectral fitting method, the spectroscopic constraint is explicitly imposed during training or iteration, which contributes to their independency of simulation dataset and hence the best performance in the APU test case.

2) Evaluation of computation efficiency

The computation efficiency is another critical evaluation metrics as the timely and immediate feedback, which is increasingly demanded in industrial applications, depends heavily on the inference speed of the model. For each of the above three networks, TABLE IV lists the model training time per epoch and the forward inference time per frame using the same device in section IV.B, as well as the model parameter size. Due to a much simpler network structure with higher efficiency, the proposed SC-LAS model enables much faster computation. It reduces the training time by factors of 15 and 184 times compared to the NNF and AOGAM models, respectively. More importantly, in terms of the inference time that determines how fast the thermochemical parameters can be extracted, the SC-LAS model improves the speed by factors of 6.17, 414 and 21,702 compared to the NNF model, the AOGAM model and the spectral fitting method, respectively. This time-efficiency advantage will benefit the SC-LAS model for its further application on large-scale tomographic systems with a large number of laser beams.

Furthermore, the model parameter size of the three models is also listed in Table IV. The proposed SC-LAS model exhibits a much light-weighted neural network for less memory usage, whose parameter size is only 1.85 % and 0.81 % compared to those of the NNF and AOGAM models, respectively.

Furthermore, the simpler-structured network with fewer model parameters enables its potential deployment on edge-computing devices [35]. The performance is evaluated by deploying the SC-LAS encoder on a Raspberry pi 4b (Cortex-A72, 4 GB), which is a representative pocket-size edge-computing platform. The result is illustrated in Table V, which demonstrates that running the SC-LAS on edge-computing devices requires very few hardware resources with power

consumption below 2 Watts, indicating its significant compatibility with industrial systems. In addition, the inference time is also 10 times shorter than the laser scan period, i.e., 1 ms in this work, indicating a neglectable latency.

V. FUTURE WORK

Although the proposed SC-LAS model has realized high performance, limitations still exist on insufficient industrial application cases, single gas species, laser beam measurement and so on. Several work may be considered in the future. Firstly, the SC-LAS model can be applied to more combustion-based systems, such as coal-fired power plants [6, 36] and waste incineration [8]. Then, combining the hyperspectral technique, the SC-LAS framework may be extended to monitor multiple combustion species simultaneously. In addition, the SC-LAS has a large potential to scale from the single laser beam to a LAS tomography system with multiple beams, which can offer spatial distribution of the target flow field. Finally, the adaptive learning can be adopted on the current SC-LAS model so that direct online flow parameters monitoring can be realized.

VI. CONCLUSION

A SC-LAS model is developed for fast and accurate extraction of thermochemical parameters for combustion-based power-generation systems. Superior to the existing supervised LAS networks, it explicitly integrates the physical constraint of the absorption spectroscopic model through the encoder-decoder structure and is trained exclusively on data sampled from industrial experiments. This unsupervised and spectroscopy-constraint manner not only frees the network training from the complicated labeling process but also enables strong generalization of the model to various industrial scenarios. Moreover, the proposed network is constructed using simple structures, i.e., 1D-CNNs and MLPs, with lightweight network parameters, which leading to high computation efficiency and further potentials on edge-computing unit deployment.

A case study on monitoring the temperature and H₂O concentration of an APU exhaust is presented to validate the proposed network. In terms of spectral features recovery, the proposed network shows the best fit with the measured WMS-2f/1f spectra, the fastest inference speed, and the lightest model structure, compared to the two state-of-the-art networks, i.e., NNF and AOGAM. The SC-LAS model also exhibits the closest plume temperature and H₂O concentration estimation to the TC reference and spectral fitting benchmark, respectively. The experimental results show the SC-LAS model effectively resolves dynamic thermochemical parameters with high accuracy, thus facilitating the control and monitoring of combustion-based power generation systems.

REFERENCES

- [1] J. Wang, Y. Xie, S. Xie, and X. Chen, "Dual Cross-Attention Transformer Networks for Temporal Predictive Modeling of Industrial Process," *IEEE Transactions on Instrumentation and Measurement*, vol. 73, pp. 1-11, 2024.
- [2] H. Deng, K. Yang, Y. Liu, S. Zhang, and Y. Yao, "Actively Exploring Informative Data for Smart Modeling of Industrial Multiphase Flow Processes," *IEEE Transactions on Industrial Informatics*, vol. 17, no. 12, pp. 8357-8366, 2021.
- [3] X. Wu, M. Wang, P. Liao, J. Shen, and Y. Li, "Solvent-based post-combustion CO₂ capture for power plants: A critical review and perspective on dynamic modelling, system identification, process control and flexible operation," *Applied Energy*, vol. 257, p. 113941, 2020.
- [4] K. Chen, J. Lin, Y. Qiu, F. Liu, and Y. Song, "Model predictive control for wind farm power tracking with deep learning-based reduced order modeling," *IEEE Transactions on Industrial Informatics*, vol. 18, no. 11, pp. 7484-7493, 2022.
- [5] Y. Lei, "Intelligent optimal framework for the industrial mining plant-wide prediction control," *IEEE Transactions on Instrumentation and Measurement*, vol. 72, pp. 1-12, 2023.
- [6] X. Han, Y. Yan, C. Cheng, Y. Chen, and Y. Zhu, "Monitoring of Oxygen Content in the Flue Gas at a Coal-Fired Power Plant Using Cloud Modeling Techniques," *IEEE Transactions on Instrumentation and Measurement*, vol. 63, no. 4, pp. 953-963, 2014.
- [7] Q. Liu, B. Zhou, R. Cheng, J. Zhang, and Y. Wang, "High Temporal Resolution Pyrometry and Velocimetry Based on Acoustic Frequency Division Multiplexing," *IEEE Transactions on Instrumentation and Measurement*, vol. 71, pp. 1-11, 2022.
- [8] J. Qiao, J. Zhou, and X. Meng, "A Multitask Learning Model for the Prediction of NO_x Emissions in Municipal Solid Waste Incineration Processes," *IEEE Transactions on Instrumentation and Measurement*, vol. 72, pp. 1-14, 2023.
- [9] J. Sun, X. Meng, and J. Qiao, "Data-Driven Optimal Control for Municipal Solid Waste Incineration Process," *IEEE Transactions on Industrial Informatics*, pp. 1-10, 2023.
- [10] Y. Liu, X. Sun, V. Sethi, D. Nalianda, Y.-G. Li, and L. Wang, "Review of modern low emissions combustion technologies for aero gas turbine engines," *Progress in Aerospace Sciences*, vol. 94, pp. 12-45, 2017.
- [11] V. E. Atasoy, A. E. Suzer, and S. Ekici, "A Comparative Analysis of Exhaust Gas Temperature Based on Machine Learning Models for Aviation Applications," *Journal of Energy Resources Technology*, vol. 144, no. 8, 2021.
- [12] A. Upadhyay *et al.*, "Tomographic imaging of carbon dioxide in the exhaust plume of largecommercial aero-engines," *Appl. Opt.*, vol. 61, no. 28, pp. 8540-8552, 2022/10/01 2022.
- [13] C. S. Goldenstein, R. M. Spearrin, J. B. Jeffries, and R. K. Hanson, "Infrared laser-absorption sensing for combustion gases," *Progress in Energy and Combustion Science*, vol. 60, pp. 132-176, 2017.
- [14] C. S. Goldenstein, C. L. Strand, I. A. Schultz, K. Sun, J. B. Jeffries, and R. K. Hanson, "Fitting of calibration-free scanned-wavelength-modulation spectroscopy spectra for determination of gas properties and absorption lineshapes," *Appl. Opt.*, vol. 53, no. 3, pp. 356-367, 2014.
- [15] W. Zhang, R. Zhang, Y. Fu, G. Enemali, J. Si, and C. Liu, "Machine Learning Based Wavelength Modulation Spectroscopy for Rapid Gas Sensing," in *2021 IEEE International Instrumentation and Measurement Technology Conference (I2MTC)*, 17-20 May 2021 2021, pp. 1-5.
- [16] L. Tian *et al.*, "Retrieval of gas concentrations in optical spectroscopy with deep learning," *Measurement*, vol. 182, p. 109739, 2021.
- [17] V. Prischepa, V. Skiba, D. Vrazhnov, and Y. V. Kistenev, "Gas mixtures IR absorption spectra decomposition using a deep neural network," *Journal of Quantitative Spectroscopy and Radiative Transfer*, vol. 301, p. 108521, 2023.
- [18] J. Sun *et al.*, "Dual gas sensor with innovative signal analysis based on neural network," *Sensors and Actuators B: Chemical*, vol. 373, p. 132697, 2022.
- [19] H. Xie, L. Xu, Y. Tan, G. Hou, and Z. Cao, "Ultra-Low Sampled and High Precision TDLAS Thermometry Via Artificial Neural Network," *IEEE Photonics Journal*, vol. 13, no. 3, pp. 1-9, 2021.
- [20] L. Tian *et al.*, "Near-infrared methane sensor with neural network filtering," *Sensors and Actuators B: Chemical*, vol. 354, p. 131207, 2022.
- [21] J. Sun *et al.*, "Adaptively Optimized Gas Analysis Model with Deep Learning for Near-Infrared Methane Sensors," *Analytical Chemistry*, vol. 94, no. 4, pp. 2321-2332, 2022.
- [22] A. Huang, Z. Cao, C. Wang, J. Wen, F. Lu, and L. Xu, "An FPGA-Based On-Chip Neural Network for TDLAS Tomography in

- Dynamic Flames," *IEEE Transactions on Instrumentation and Measurement*, vol. 70, pp. 1-11, 2021.
- [23] Y. Wang, S. Chen, Q. Kong, and J. Gao, "Research on CO concentration detection based on deep learning and TDLAS technology," *Optics and Lasers in Engineering*, vol. 181, p. 108420, 2024/10/01/ 2024.
- [24] H. Xiong *et al.*, "Neural Network Based Aliasing Spectral Decoupling Algorithm for Precise Mid-Infrared Multicomponent Gases Sensing," *ACS sensors*, vol. 9, no. 9, pp. 4906-4914, 2024.
- [25] M. Mhanna, J. Rochussen, and P. Kirchen, "An ML-Enhanced Laser-Based Methane Slip Sensor Using Wavelength Modulation Spectroscopy," *ACS sensors*, 2025.
- [26] I. E. Gordon *et al.*, "The HITRAN2020 molecular spectroscopic database," *Journal of Quantitative Spectroscopy and Radiative Transfer*, vol. 277, p. 107949, 2022.
- [27] Y. Fu *et al.*, "Hybrid Model-Driven Spectroscopic Network for Rapid Retrieval of Turbine Exhaust Temperature," *IEEE Transactions on Instrumentation and Measurement*, vol. 72, pp. 1-10, 2023.
- [28] J. Xia *et al.*, "FPGA-Accelerated Distributed Sensing System for Real-Time Industrial Laser Absorption Spectroscopy Tomography at Kilo-Hertz," *IEEE Transactions on Industrial Informatics*, 2023, doi: 10.1109/TII.2023.3292971[early access].
- [29] G. Enemali, R. Zhang, H. McCann, and C. Liu, "Cost-Effective Quasi-Parallel Sensing Instrumentation for Industrial Chemical Species Tomography," *IEEE Transactions on Industrial Electronics*, vol. 69, no. 2, pp. 2107-2116, 2022.
- [30] G. B. Rieker, J. B. Jeffries, and R. K. Hanson, "Calibration-free wavelength-modulation spectroscopy for measurements of gas temperature and concentration in harsh environments," *Appl. Opt.*, vol. 48, no. 29, pp. 5546-5560, 2009.
- [31] C. S. Goldenstein, I. A. Schultz, J. B. Jeffries, and R. K. Hanson, "Two-color absorption spectroscopy strategy for measuring the column density and path average temperature of the absorbing species in nonuniform gases," *Appl. Opt.*, vol. 52, no. 33, pp. 7950-7962, 2013.
- [32] S. Kiranyaz, O. Avci, O. Abdeljaber, T. Ince, M. Gabbouj, and D. J. Inman, "1D convolutional neural networks and applications: A survey," *Mechanical Systems and Signal Processing*, vol. 151, p. 107398, 2021.
- [33] R. Zhang *et al.*, "A fast sensor for non-intrusive measurement of concentration and temperature in turbine exhaust," *Sensors and Actuators B: Chemical*, vol. 396, p. 134500, 2023.
- [34] D. P. Kingma and J. Ba, "Adam: A method for stochastic optimization," *arXiv preprint arXiv:1412.6980*, 2014.
- [35] W. Dai, H. Nishi, V. Vyatkin, V. Huang, Y. Shi, and X. Guan, "Industrial Edge Computing: Enabling Embedded Intelligence," *IEEE Industrial Electronics Magazine*, vol. 13, no. 4, pp. 48-56, 2019.
- [36] J. Li *et al.*, "In situ, portable and robust laser sensor for simultaneous measurement of ammonia, water vapor and temperature in denitrification processes of coal fired power plants," *Sensors and Actuators B: Chemical*, vol. 305, p. 127533, 2020.